







# Experimental Evaluation of Fluid Connectivity in Two-Phase Flow in Porous Media During Drainage

Samaneh Vahid Dastjerdi<sup>1,2</sup> , Nikolaos Karadimitriou<sup>1,2</sup> , S. Majid Hassanizadeh<sup>2,3</sup> , and Holger Steeb<sup>1,2</sup> 

<sup>1</sup>Institute for Applied Mechanics (MIB), University of Stuttgart, Stuttgart, Germany, <sup>2</sup>SC SimTech, University of Stuttgart, Stuttgart, Germany, <sup>3</sup>Department of Earth Sciences, Utrecht University, Utrecht, The Netherlands

### Key Points:

- A large number of two-phase displacement microfluidic experiments under different boundary conditions are performed
- A code has been developed in order to spatially and temporally resolve the experiments with high accuracy
- Including both connectivity and interfacial area as state variables in two-phase flow continuum theories improves modeling hysteresis

### Correspondence to:

S. Vahid Dastjerdi,  
[samaneh.vahiddastjerdi@mechbau.uni-stuttgart.de](mailto:samaneh.vahiddastjerdi@mechbau.uni-stuttgart.de)

### Citation:

Vahid Dastjerdi, S., Karadimitriou, N., Hassanizadeh, S. M., & Steeb, H. (2022). Experimental evaluation of fluid connectivity in two-phase flow in porous media during drainage. *Water Resources Research*, 58, e2022WR033451. <https://doi.org/10.1029/2022WR033451>

Received 16 AUG 2022

Accepted 20 OCT 2022

**Abstract** This study aims to experimentally investigate the possibility of combining two extended continuum theories for two-phase flow. One of these theories considers interfacial area as a separate state variable, and the other explicitly discriminates between connected and disconnected phases. This combination enhances our potential to effectively model the apparent hysteresis, which generally dominates two-phase flow. Using optical microscopy, we perform microfluidic experiments in quasi-2D artificial porous media for various cyclic displacement processes and boundary conditions. Specifically for a number of sequential drainage processes, with detailed image (post-)processing, pore-scale parameters such as the interfacial area between the phases (wetting, non-wetting, and solid), and local capillary pressure, as well as macroscopic parameters like saturation, are estimated. We show that discriminating between connected and disconnected clusters and the concept of the interfacial area as a separate state variable can be an appropriate way of modeling hysteresis in a two-phase flow scheme. The drainage datasets of capillary pressure, saturation, and specific interfacial area, are plotted as a surface, given by  $f(P^c, s^w, a^{wn}) = 0$ . These surfaces accommodate all data points within a reasonable experimental error, irrespective of the boundary conditions, as long as the corresponding liquid is connected to its inlet. However, this concept also shows signs of reduced efficiency as a modeling approach in datasets gathered through combining experiments with higher volumetric fluxes. We attribute this observation to the effect of the porous medium geometry on the phase distribution. This yields further elaboration, in which this speculation is thoroughly studied and analyzed.

## 1. Introduction

The identification and verification of a complete constitutive continuum theory, which includes an extended set of state variables and related constitutive models, for two-phase flow in porous media have been fields of active research for the last decades. Addressing the behavior of capillary pressure versus saturation, which is process- and history-dependent, also known as hysteretic, belongs to these theoretical (Mecke & Arns, 2005; Miller et al., 2019; Spiteri et al., 2008), numerical (Armstrong et al., 2016; Joekar-Niasar et al., 2013), and experimental (Herring et al., 2013; Tsakiroglou et al., 2003) attempts. The determination of ways to lift this ambiguity have been “hot” topics related to two-phase flow in porous media. Various efforts have been made to address this hysteretic nature with the introduction of additional state variables, and the establishment of an extended continuum theory (Hilfer, 2006b; Hassanizadeh & Gray, 1993; Hilfer & Doster, 2010). Implementing such extended continuum theories in real-life applications of two-phase flow for various scientific, engineering, and industrial purposes, with a vast socioeconomic impact, is crucial. Such applications include, but are not limited to, geological carbon sequestration (Bachu, 2000; Benson & Cole, 2008; White et al., 2003), enhanced oil recovery (Alvarado & Manrique, 2010; Muggeridge et al., 2014), and remediation of contaminated groundwater/soil from a non-aqueous phase liquid (Powers et al., 1992; Quintard & Whitaker, 1994). A physically consistent and adequate description of the underlying physical processes during two-phase flow would improve our predictive capabilities in all these applications. Moreover, such theories could help us enhance the efficiency of the process itself by fine-tuning the corresponding parameters of the system. Among these parameters, one can name the physical and chemical properties of the fluids and the solids involved.

So far, none of the proposed theories have been validated for general conditions; neither numerically nor experimentally. For instance, using concepts of volume averaging and rational continuum-thermodynamics, Hassanizadeh and Gray (1990, 1993) develop an extended macroscopic theory for two-phase flow. Among others, they argue that the multi-valuedness of capillary pressure for a given saturation is because fluids can be

© 2022. The Authors.

This is an open access article under the terms of the [Creative Commons Attribution License](https://creativecommons.org/licenses/by/4.0/), which permits use, distribution and reproduction in any medium, provided the original work is properly cited.

distributed in the pores in many different ways at a certain saturation. Thus, a macroscale quantity (read a state variable) is needed to characterize different fluids configurations at any given saturation (Hassanizadeh, 2015). Also, they argue that the dynamics of interfaces are distinctly different from the dynamics of phases and are governed by different equations. As saturation and fluid pressures are volumetric measures, a new state variable should pertain to interfacial configurations. In fact, when one starts at the pore scale, governing equations are needed not only for phases but also for interfaces. Similarly, at the macroscale, one should have governing and state variables equations for both phases and interfaces (Gray & Hassanizadeh, 1989; Marle, 1982). In the continuum theory developed by Hassanizadeh and Gray (1990), macroscale capillary pressure is found to be the derivative of Helmholtz free energy of all phases and interfaces with respect to saturation. The specific interfacial areas between the three phases (wetting and non-wetting fluids and the solid structure) naturally appear as additional state variables in their macroscale theory of two-phase flow. In particular, they find that in general capillary pressure should be a function of these specific interfacial areas as well as saturation

$$P^c = f(a^{ns}, a^{ws}, a^{wn}, s^w). \quad (1)$$

Here,  $P^c$  is the macroscale capillary pressure,  $a^{\alpha\beta}$  is the specific interfacial area between phase  $\alpha$  and phase  $\beta$ . With  $s^{nw}$  being the saturation of non-wetting phase, it is known that  $s^w + s^{nw} = 1$ . For perfectly wettable porous media, the variation of  $a^{ws}$  may be assumed negligible and the role of  $a^{ns}$  is insignificant. Thus, the set of state variables reduces to the interfacial area between the wetting and the non-wetting phase by assuming that  $a^{ws} + a^{ns}$  is a constant and  $a^{ns} = 0$  except for a minimal saturation of the wetting phase. This leads to

$$P^c = f(a^{wn}, s^w). \quad (2)$$

The practical implementation of this extended continuum approach yields that instead of assuming capillary pressure to be a function of a single variable (saturation), to characterize the system, one needs to plot capillary pressure versus saturation and interfacial area as a three-dimensional surface. In theory, the resulting surface should accommodate any potential combination between the three state variables (capillary pressure, saturation, and interfacial area). Assuming that the combination of the fluids and the porous medium remains unaltered, the extended theory of two-phase flow proposed by Hassanizadeh and Gray (1993) should hold under any boundary conditions.

In another attempt, Hilfer (2006a, 2006b) presents a phenomenological approach without including the interfacial area between phases. He addresses capillary pressure as a thermodynamic response function of the theory and introduces trapped, or residual, saturation as an extra variable in his continuum theory for capillarity in porous media. To reflect the dependency of residual saturation on the initial and boundary conditions of the process, he refers to residual saturation as the non-percolating saturation of a fluid phase. He distinguishes between the percolating and non-percolating saturation of the phase. In his work, the volume fraction of the phase clusters connected to the permeable domain boundaries is considered percolating saturation of the phase. He also claims that even though there are some strong assumptions in his phenomenological theory, the resulting theory is more general than the established commonly used flow theories (Bear, 1972).

In recent years, numerical and experimental efforts have been made in order to evaluate the validity of the mentioned continuum theories (Chen et al., 2007; Doster & Hilfer, 2014; Gao et al., 2021; Held & Celia, 2001; Hilfer & Doster, 2010; Hilfer et al., 2015; Joekar-Niasar et al., 2008; Joekar-Niasar et al., 2013; Joekar-Niasar & Hassanizadeh, 2011; Karadimitriou et al., 2013; Niessner & Hassanizadeh, 2008, 2009; Zhuang, Bezerra Coelho, et al., 2017; Zhuang, Hassanizadeh, et al., 2017). Although some advancements are made for quasi-static conditions, none of them are proven to be unconditionally holding or practically applicable. For example, the investigations of the extended theory of Hassanizadeh et al. show that, under quasi-static conditions, the inclusion of the interfacial area as a separate state variable helps to model the hysteretic nature of the capillary pressure-saturation relationship to a reasonable extent (Chen et al., 2007; Cheng et al., 2004; Held & Celia, 2001; Joekar-Niasar et al., 2008; Karadimitriou et al., 2013). However, the experimental verification of this theory under transient flow conditions is proven to be a more difficult task. In particular, in the case of pore-scale experiments or micro X-ray computed tomography ( $\mu$ XRCT) measurements, detailed information in time and space is needed. To gather such information through visualization, the imaging needs to be swift and real-time, especially for fast transient events. Another challenge is the combination of imaging with the optical properties of a porous medium. For opaque porous media (such as a small column), successful attempts have been made to visualize displacement

processes and extract pore-scale information with the use of  $\mu$ XRCT (Armstrong et al., 2012; Bartels et al., 2019; Culligan et al., 2004). Nonetheless, given the limitations of the imaging technique itself, it is intrinsically challenging to perform dynamic experiments with an adequate imaging rate to capture the pore-scale dynamics. Although the technology that comes with  $\mu$ XRCT has progressed significantly (both in terms of image quality and acquisition times), a synchrotron facility is needed to take advantage of these advancements. Since the need for fast and high-resolution imaging is elevated for studying dynamic pore-scale effects, in some cases, one complete image of the porous domain has to be performed in less than one second, which jeopardizes the resolution of the images and their quality. Due to these limitations, optical microscopy is the dominant approach for fast imaging since it is feasible in a laboratory environment and can be performed flexibly. Therefore, it has been used vastly in experimental studies of transient flow conditions in porous media (Pyrak-Nolte et al., 2008; Weinhardt et al., 2021; Yiotis et al., 2021).

Taking advantage of optical microscopy, Karadimitriou et al. (2014) are the first to investigate the theory proposed by Hassanizadeh and Gray with the use of microfluidics and under transient conditions, with real-time imaging. Their micromodel experiments show that under quasi-static conditions, experimental data points of  $a^{wn}$ ,  $P^c$ , and  $s^w$  from a series of drainage and imbibition cycles fall on a unique surface within a reasonable experimental error. However, that is not found to be the case under transient flow conditions. Karadimitriou et al. attribute the mismatch, which is growing for increasing boundary pressures, to the rise in disconnection of the non-wetting phase, occurring due to surging competition between surface and viscous forces. Their experimental results are in agreement with the numerical results from Joekar-Niasar and Hassanizadeh (2011).

In recent years, some researchers have proposed another macroscale state variable to account for the role of phase topology in modeling approaches for two-phase flow in porous media. This characteristic measure, known as Euler characteristic number, is a natural characterization measure of phase discontinuities, originated in mathematics. Euler characteristic number ( $\chi$ ) for a three-dimensional body is calculated as the linear combination of Betti numbers,  $\chi = b_0 - b_1 + b_2$ , where  $b_0$  is the number of isolated objects,  $b_1$  is the number of redundant loops, and  $b_2$  is the number of cavities. Several theoretical (Armstrong et al., 2019; Miller et al., 2019), numerical (McClure et al., 2016, 2018, 2020), and experimental (Armstrong et al., 2016; Herring et al., 2013; Ott et al., 2020; Schlüter et al., 2016) studies have addressed the consideration of the Euler characteristic number as a state variable. Their studies show that Euler characteristic number can provide an improved indication of two-phase flow and its relevant pore-scale phenomena. For example, McClure et al. (2018, 2020) developed some geometric state functions for Euler characteristic number by following principles of integral geometry. However, there is no consensus in the literature regarding a universal applicability of the Euler characteristic number for modeling two-phase flow, with respect to the phases involved. To a more fundamental level, the Euler characteristic number ends up being an abstract measure which occasionally cannot be translated to a physical meaning. In addition, the Euler characteristic number is a topological measure that is hard to acquire without detailed visual information from displacement configurations (Herring et al., 2019), especially at the macroscopic scale. On the other hand, the interplay of topological measures such as Euler characteristic number (degree of connectivity of phase clusters to each other) as well as geometrical measures (size and shape of the pores) affect percolating of the phases. Thus, we believe considering connectivity of the clusters to the flow path can encapsulate both global and local information and should be studied further.

Among the experimental and numerical investigations of two-phase displacement events some, such as Armstrong et al. (2012) and Herring et al. (2017), considered connectivity of the clusters to the flowing phase in their investigations (as approached in the theory of Hilfer (2006a, 2006b)). It should be noted that the connectivity, as regarded by Armstrong et al. and Herring et al. and as included in the modeling approach of Hilfer, is not necessarily what is described with the concept of Euler characteristic number. The former differentiates between the clusters based on their participation in the flow. The latter provides a measure of connectivity in one phase regardless of the flow. The results of their work show that there is a difference in the local curvature of the interfaces connected to the flow and the interfaces disconnected from the flow under equilibrium state. Based on pressure values read from pressure transducers, Armstrong et al. and Herring et al. calculate the pressure difference between wetting and nonwetting phase and compare it with the average capillary pressure calculated from local curvature of the imaged fluid-fluid interfaces (through Young-Laplace equation). They conclude that under equilibrium state and during imbibition, these two pressures are in good agreement, only if the interfaces disconnected from the flow are excluded from calculation of capillary pressure. This outcome emphasizes the importance of considering the

connection to the flow, when defining the capillary pressure during flow in porous media. However, in the experimental work Armstrong et al. and Herring et al. both present, XRCT imaging is employed.

For XRCT imaging outside of a synchrotron facility, the transient resolution of imaging is very limited. Typically, it takes significant time to get a whole 3D scan of a porous medium under flow conditions; in the order of tens of seconds in a good scenario. This imposes a constraint regarding the speed at which displacement events take place, and their effective imaging. This means nearly equilibrium states are preferred or there is poor time resolution and/or limited amount of displacement events. Moreover, either spatial resolution of the images needs to be sacrificed, which prevents the detection of some microscale features such as wetting films, or size of the domain under investigation. Considering these limitations discussed, the investigations of Armstrong et al. and Herring et al. can benefit from transient state information gathered with methods that allow time-resolved flow experiments. As mentioned before, optical microscopy allows for high spatial and temporal resolution imaging, independently of flow conditions, which can provide the type of complementary information, we look for.

In this work, we combine microfluidic experiments, optical microscopy, and image processing techniques in order to perform a large number of two-phase flow experiments under different boundary conditions (thus, different capillary numbers). We are able to obtain desired spatial and temporal resolution in our experiments and carry out high accuracy investigations, which is to test the hypothesis of a potential synthesis of the theories proposed by Hassanizadeh and Gray (1990, 1993) and Hilfer (2006a, 2006b). The data allows us to study the role of disconnected phases (non-percolating) in the theory that includes interfacial area as a separate state variable in two-phase flow models. To the best of our knowledge, this is the first microfluidic experimental investigation which addresses merging of two existing continuum-theories, in order to overcome their dependency on the boundary conditions, when they are applied individually. For this purpose, flux-controlled microfluidic experiments consisting of sequential drainage and imbibition cycles are carried out, and images of the related phase distribution of the fluids are recorded. The number of cycles assures that the experiments are not only considering primary drainage and main imbibition, but also a considerable number of scanning events, which induce sequential disconnection and reconnection of clusters. Subsequently, the images are processed, and the interfacial area between the three phases, as well as the curvature and contact angle of the terminal menisci, are extracted. Using the Young-Laplace equation, the local (micro-scale) capillary pressure associated with each wetting/non-wetting interface is calculated and averaged over all fluid-fluid interfaces. Then, a simple constitutive formula for the interfacial area as a function of phase saturation and capillary pressure is fitted to the experimental data. To address the connectivity of phases, two approaches are adopted. In one approach, all the terminal menisci between the wetting and non-wetting phases for all displacement processes are included in the analysis and averaging. In the other approach, we include only those interfaces that are formed between the percolating phase and the other fluid. The goodness of fit for the two approaches then compared by utilizing the  $R^2$  parameter to see if and how taking the disconnected clusters out of the calculations helps describe a two-phase cyclic displacement process with a single  $P^c - s^w - a^{wn}$  surface.  $R^2$  is a statistical measure that illustrates the strength of the relationship between the model and the variable on a 0%–100% scale.

## 2. Materials and Methods

### 2.1. Experimental Setup

The experimental setup consists of a microfluidic chip bearing a flow network with microscale features, also referred to as a micromodel, an open-air microscope, and a syringe pump. A schematic view of the setup is shown in Figure 1.

Various parts of the experimental setup will be thoroughly presented in the coming sections.

#### 2.1.1. Microfluidic Cell

A glass micromodel with cylindrical grains serves as the porous medium in the microfluidic experiments. This type of micromodels is commercially available from Micronit® GmbH, with the flow network being wet-etched in glass (Damodara et al., 2021). In this method, the desired design of the microfluidic cell (Figure 2a) is made out of an acid-resistant material, which serves as a mask in the production process. A glass plate covered with the mask is subsequently exposed to an acid that causes the glass to dissolve selectively, based on the mask used, and form channels of a certain depth. In this work, the depth of the cell is 35  $\mu\text{m}$ , and its pore sizes are between 75 and

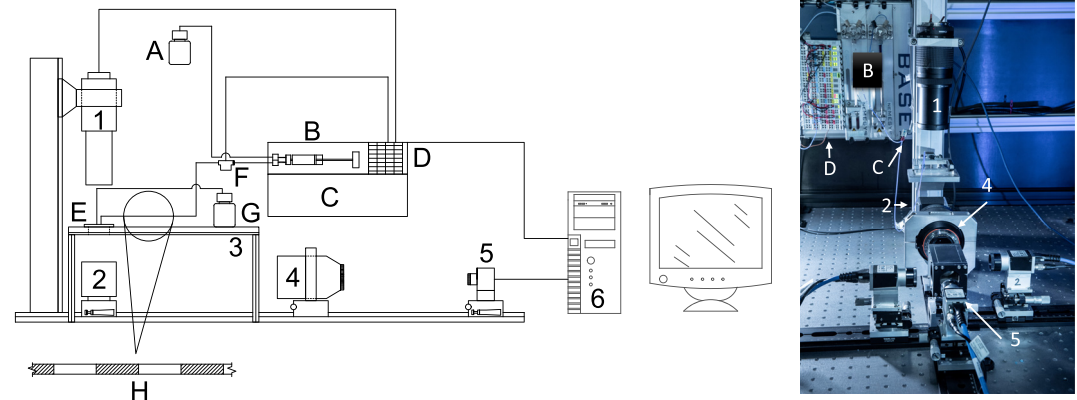


**Figure 1.** Experimental setup: Open air microscope (1–6); 1) Light source: 1W LED light source emitting at 590 nm mounted on an objective lens with F/3.2–135 mm; 2) Prism: 50 mm Edmund Optics®; 3) Stage for the microfluidic cell; 4) Lens: Sigma® F/1.8–135 mm DG HSM telephoto; 5) Camera: 5 Mpx, 23 fps, Basler® acA2440-20gm; 6) Computer. Flow setup (A–G); (A) Reservoir for the fluids; (B) Syringe pump: CETONI® neMESYS 1000N; (C) CETONI base module 120; (D) CETONI® I/O module 16-bit; (E) Microfluidic cell; (F) Pressure sensor (Elveflow® MPS03, range 0–70 mbar); (G) Outlet reservoir; (H) Fluid layers in the inlet tube; hatched in black is the colored water and white is the transparent oil. Photo is taken by Uli Regenscheit Fotografie.

250  $\mu\text{m}$  with a mean value of 180  $\mu\text{m}$ . The flow network is a periodic one, with the replication of a pore network pattern twice in the vertical and three times in the horizontal direction (Figures 2a and 2c).

### 2.1.2. Visualization and Flow Monitoring

The visualization setup is a modified version of the one introduced by Karadimitriou et al. (2012). In our case, only one camera is used. The components of the microscope are a 1W LED light source emitting at 590 nm mounted on a F/3.2–135 mm Canon objective lens, an Edmund Optics® prism, a stage for the microfluidic cell, a Sigma® F/1.8–135 mm tele-lens, and a 5 Mpx, 23 fps, Basler® acA2440-20gm monochrome camera (Figure 1). This visualization setup, given the properties of the optics and the camera, is capable of acquiring images from the microfluidic experiments at a resolution ranging from 0.5 to 20  $\frac{\mu\text{m}}{\text{pixel}}$ , and an acquisition rate ranging from 0.07 to 23 fps. The image acquisition rates based on the needs of the experiments presented here and the number of processed images and the image size are listed in Table 1. It should be noted that the sensor field of view has dimensions of 2,448  $\times$  2,050 pixels originally. However, the region of interest is cut out for further processing. The space resolution needed to have the whole porous domain of the cell in the view field is  $\sim 8.3 \mu\text{m}/\text{pixel}$ .

The fluxes at the inlet are generated and controlled by a computer-operated CETONI® syringe pump (mid-pressure CETONI® neMESYS 1000N, BASE 120, 16-bit DAQ I/O module). QMixElements® is used as the communication software between the computer and the pump. Furthermore, the experimental parameters, such as the volu-

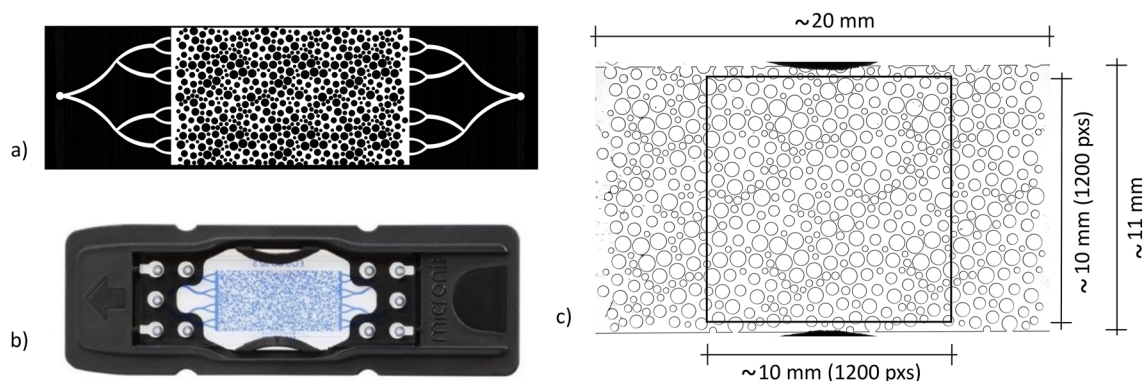


**Figure 2.** Microfluidic cell: (a) Design: Flow channels in white, (b) Final product saturated with blue ink, (c) Porous domain (Under microscope with resolution of  $\sim 8.3 \mu\text{m}/\text{pixel}$ ).

**Table 1**  
*Image Acquisition Settings*

	Volumetric flux ( $\mu$ l/min)	Ca <sup>a</sup> (–)	Image acquisition rate (fps)	Number of processed images	Image size (Pixels)
Exp. 1	0.03	10 <sup>-7</sup>	1	3,839	2,448 × 1,461
Exp. 2	0.3	10 <sup>-6</sup>	5	3,851	2,448 × 1,461
Exp. 3	3	10 <sup>-5</sup>	10	3,877	2,448 × 1,446

*Note.* where  $q$  is the Darcy velocity (m/s),  $\mu$  is viscosity of the injected fluid (Ns/m<sup>2</sup>), and  $\sigma^{wn}$  is the surface tension between the two fluids (N/m).

<sup>a</sup>Capillary number:  $Ca = \frac{\mu q}{\sigma^{wn}}$ .

metric flux, are defined, and the induced boundary pressures are measured and logged through the communication software using a 16-bit DAQ I/O module.

## 2.2. Two-Phase Flow Experiments

The two immiscible phases, water and Fluorinert (3M Fluorinert™ FC-43 Liquid), are chosen in the experiments as the wetting and non-wetting phases, respectively. In order to create the necessary contrast between the two colorless fluids, water is mixed with water-based ink (Talens Ecoline 578 Liquid Watercolor) at a volume ratio of 50%. The viscosity of water and Fluorinert are known to be 1 and 4.7 Pa.s, respectively. The density of water is 997 kg/m<sup>3</sup> and density of Fluorinert is 1,860 kg/m<sup>3</sup>. As mentioned, the experiments are flow-controlled, and the capillary number of the primary drainage is fixed to 10<sup>-5</sup>, 10<sup>-6</sup>, and 10<sup>-7</sup>, by setting the volumetric fluxes to 0.03, 0.3, and 3  $\mu$ l/min, respectively (Table 1).

Twelve equivolume Fluorinert and water pulses are introduced into the inlet tube, without the microfluidic cell being attached, to realize 12 sequential displacement processes. The inlet tube, filled with the fluid layers in it, is sketched in Figure 1 (item H). The volume of each pulse is 12  $\mu$ l, which is five times the micromodel pore volume ( $\sim$ 2.4  $\mu$ l), in order to ensure a steady-state after the breakthrough. Then, the inlet tube with the 12 pulses is connected to the fully saturated with water micromodel and the injection is initiated at the volumetric fluxes mentioned earlier. The introduction of the fluid layers into the cell, induces 12 displacement processes of primary drainage, main imbibition, and 10 scanning curves. Furthermore, we measure and record the pressure before the inlet of the cell while having a constant back pressure (as a constant water head equal to  $\sim$ 1 kPa) at the outlet to monitor the stability of the process.

## 2.3. Image Processing

In order to extract quantitative information from our investigations, an image-processing tool is developed in MATLAB® (2019). This tool is employed to segment and analyze the images acquired during the real-time visualization of our two-phase flow experiments.

As the first step, images are segmented to delineate the solid skeleton and wetting and non-wetting phases. To distinguish between the solid skeleton and the non-wetting phase, which are both colorless, a mask is subtracted from each image. The mask is an image of the microfluidic cell fully saturated with dyed water at the initial stage of each experiment. Afterward, the subtraction result is segmented and assigned to the desired phases using multi-thresholding methods. The thresholding procedure is carried out using MATLAB functions such as `multithresh`, and `imquantize`, or self-developed functions. To pursue the objectives of this investigation, the non-wetting and wetting phase clusters that are disconnected from the bulk flow need to be distinguished. Examples of a segmented image and the disconnected clusters of the non-wetting phase are shown in Figures 3b and 3c, respectively. A cluster is considered to be connected if it has connections to the inlet boundary of the porous domain, following the definition used in Hilfer (2006a) regarding the percolation of a cluster. From now on, and for consistency reasons, the clusters connected to the inlet of the porous domain will be addressed as the connected clusters. Next, the saturation of the wetting and non-wetting phase is calculated. The interfaces between the three phases are identified. The length of each interface is determined as the cumulative distance between the neighboring points (Figure 3d).

Moreover, the contact angle of each end of the interface with the solid skeleton is calculated. It is observed that the two angles on the two ends of an interface could be different. To have a single contact angle for the interface, we take the average of the two contact angles. For the in-depth contact angle of the interface, the mean value of all the calculated contact angles in the  $x$ - $y$  plane is calculated separately for drainage and imbibition. Two other parameters obtained from the images are the chord length and radius of curvature for each interface. The chord length of the interface is defined as the Euclidean difference between the two endpoints of the interface, which is equal to the depth of the cell in the  $y$ - $z$  plane. The curvature is defined as  $1/r$ , where  $r$  is the planar radius of curvature of an interface, determined as the radius of a circle fitted to the interface using the method suggested

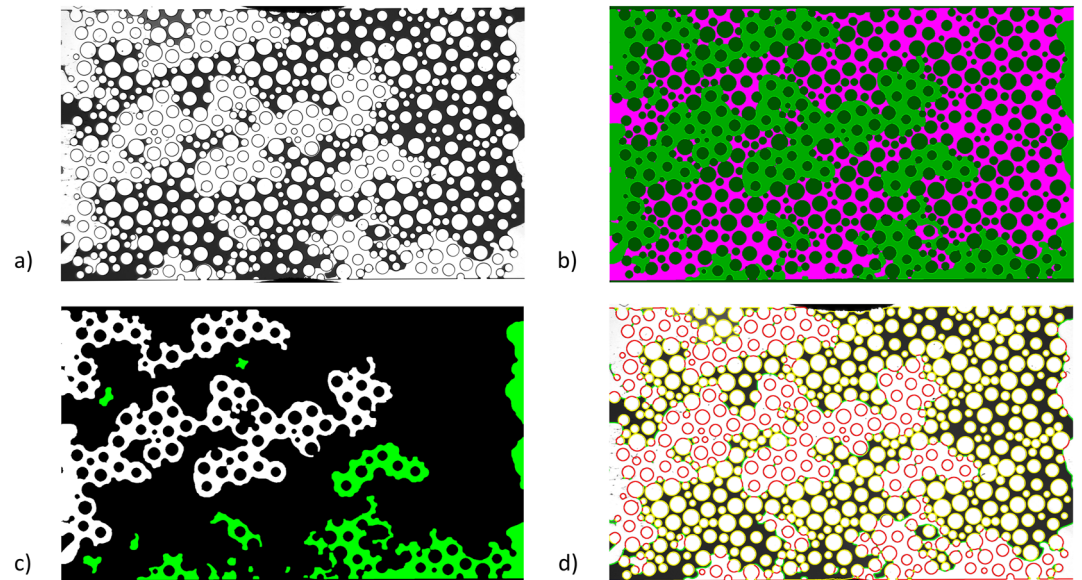


**Figure 3.** Image processing: (a) Original image, (b) Segmentation into three phases: light green representing the non-wetting phase, the wetting phase, and the solid skeleton, respectively, (c) Distinguishing connected clusters and not-connected clusters in the non-wetting phase, (d) Interfaces between the three phases: red: non-wetting—solid, yellow: wetting—solid, green: non-wetting—wetting.

by Pratt (1987) and a MATLAB code developed by Chernov (2021), in the  $x$ - $y$  plane. These parameters are substituted in the Young-Laplace equation (Equation 3) to calculate the capillary pressure associated with each interface.

As mentioned in Section 2.1.2, the original images have dimensions of  $2,448 \times 2,050$  pixels at a resolution of  $\sim 8.3 \mu\text{m}/\text{pixel}$ . We investigate the size of Representative Elementary Volume (REV) for both specific interfacial area ( $1/\text{m}$ ) and the mean curvature ( $1/\text{m}$ ) in form of their quantity as a function of domain size, as carried out in the literature (Bear, 1972; Hassanizadeh & Gray, 1979). The REV size in our investigations is determined to be in the order of  $1,200 \times 1,200$  pixels ( $\sim 10 \times 10 \text{ mm}$ ). The porous domain dimensions in our experiments are ca.  $1,460 \times 2,448$  pixels ( $\sim 11 \times 20 \text{ mm}$ ). So, the middle part of the micromodel qualifies as at least one REV.

#### 2.4. Post-Processing

In order to compare and test the validity of macroscopic theories, quantities like saturation, interfacial area, and capillary pressure should be evaluated at the REV scale. The capillary pressure is locally calculated using the Young-Laplace equation for each interface and subsequently averaged over the interfacial area for the REV-scale capillary pressure calculation. In our micromodel, the Young-Laplace equation may be written as

$$p_i^c = \sigma^{wn} \left( k_i + 2 \frac{\cos \alpha}{d} \right), \quad (3)$$

Where  $p_i^c$  is the capillary pressure at interface  $i$ ,  $\sigma^{wn}$  is the surface tension between Fluorinert and water equal to  $55 \text{ mN/m}^2$ ,  $k_i$  is the curvature of interface  $i$  in the  $x$ - $y$  plane ( $1/\text{m}$ ),  $\alpha$  is the average in-depth contact angle (in the  $y$ - $z$  plane), and  $d$  is the depth of the cell (here  $35 \mu\text{m}$ ). The value of the in-depth contact angle is determined to be  $56^\circ$  and  $58^\circ$  during drainage and imbibition, respectively, following the procedure described above. As mentioned, from the local capillary pressures calculated for each interface, an average capillary pressure is calculated associated with each image using Equation 4 (Whitaker, 2013).

$$p_{REV}^c = \frac{\sum (p_i^c A_i^{wn})}{\sum A_i^{wn}}, \quad (4)$$

Where  $A_i^{wn}$  is the area of interface  $i$  ( $\text{m}^2$ ), calculated through

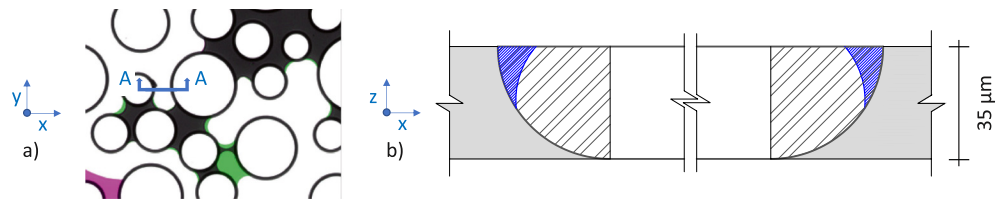


**Figure 4.** Wetting phase connectivity in the microfluidic experiments: (a) Volume change in a wetting cluster during imbibition: Marked in green is the pore space drained during imbibition, (b) In-depth view of section A-A in chemically etched micromodels: A pore and hypothetical corner flow extensions (hatched in black is the shadow seen as the solid wall in microscopy images, hatched in blue is the wetting phase remaining in channel corners and hatched in gray is the solid skeleton).

$$A_i^{wn} = \frac{L_i d}{\cos \alpha} \left( \frac{\pi}{2} - \alpha \right). \quad (5)$$

Here  $L_i$  is the length of each interface (m), calculated by image processing. The data points related to the saturation of the invading phase, the area of wetting/non-wetting interfaces, and the capillary pressure associated with the interfaces, are collected for all clusters as well as the connected clusters only.

As the fitting function for the data points of saturation, specific interfacial area, and capillary pressure, we use a modified version of the one proposed in Karadimitriou et al. (2013) and Joekar-Niasar and Hassanizadeh (2012). Here, the non-wetting phase saturation is selected to be the saturation of the invading phase, meaning the non-wetting phase saturation for drainage and saturation of the wetting phase for imbibition. Additionally, to make the equation consistent in terms of units, we divide the corresponding capillary pressures with the atmospheric one, considered constant throughout the experiments. Equation 6 shows the expression used to fit the experimental data by tuning parameters  $a$ ,  $b$ ,  $c$ ,  $d$

$$a^{wn} = a (s^{inv})^b (1 - s^{inv})^c \left( \frac{P_{REV}^c}{p^{atm}} \right)^d, \quad (6)$$

Where  $a^{wn}$  is the specific interfacial area (1/m), calculated as the total interfacial wetting/non-wetting area (cumulative  $A^{wn}$  in REV-scale) divided by the bulk volume of the porous medium (in our case it is  $11 \text{ mm} \times 20 \text{ mm} \times 35 \text{ }\mu\text{m}$ ).  $s^{inv}$  is the saturation of the fluid which is entering the porous medium and is exercising the active forces on the flow front.  $p^{atm}$  is the atmospheric pressure and is considered to be constant in all experiments. Parameter  $a$  has the unit of 1/m, and parameters  $b$ ,  $c$  and  $d$  are dimensionless.

The motivation behind the adoption of this equation to proceed with the fitting, as also explained in Karadimitriou et al. (2013), and Joekar-Niasar and Hassanizadeh (2012), is that this equation satisfies two pre-requisites: (a) for saturation of zero or one, the interfacial area should be zero, and (b) for a capillary pressure of zero, the interfacial area should also be zero given the wetting properties of the porous medium.

Although the experiments are carried out for sequential drainage and imbibition, the results presented here are from the drainage processes. This is because of the noticeable corner/film flow, which affects the connectivity of the wetting phase. The shape of the flow channels, typical for chemically etched microstructures, and the wetting properties of glass enable and strengthen such flow paths in the flow channels. Although there is strong evidence for the mentioned connectivity (Figure 4a), the extent of this connectivity cannot be estimated from the images. As it can be seen in Figure 4b, the shadow formed around the solid pillars (hatched in black), which is due to the curved walls, is preventing the corner/film flow (hatched in blue) from being captured in the images. However, the area which is marked in green in Figure 4a, is a pore which is drained during flow without any visible connections to the rest of the wetting phase. This volume change provides evidence of a corner/film connection, which facilitates (in the cluster shown in Figure 4) the drainage of the wetting phase for more than 70% of its volume. Consequently, defining a disconnected cluster and its volume for the wetting phase becomes a risky process. Since our ability to identify a cluster as such is very limited, the corresponding results are seriously affected by any assumptions in this regard. To quantify the saturation of the wetting phase accommodated in the corners in our experiments, further investigations using other imaging techniques such as  $\mu\text{XRCT}$  could be used. However,



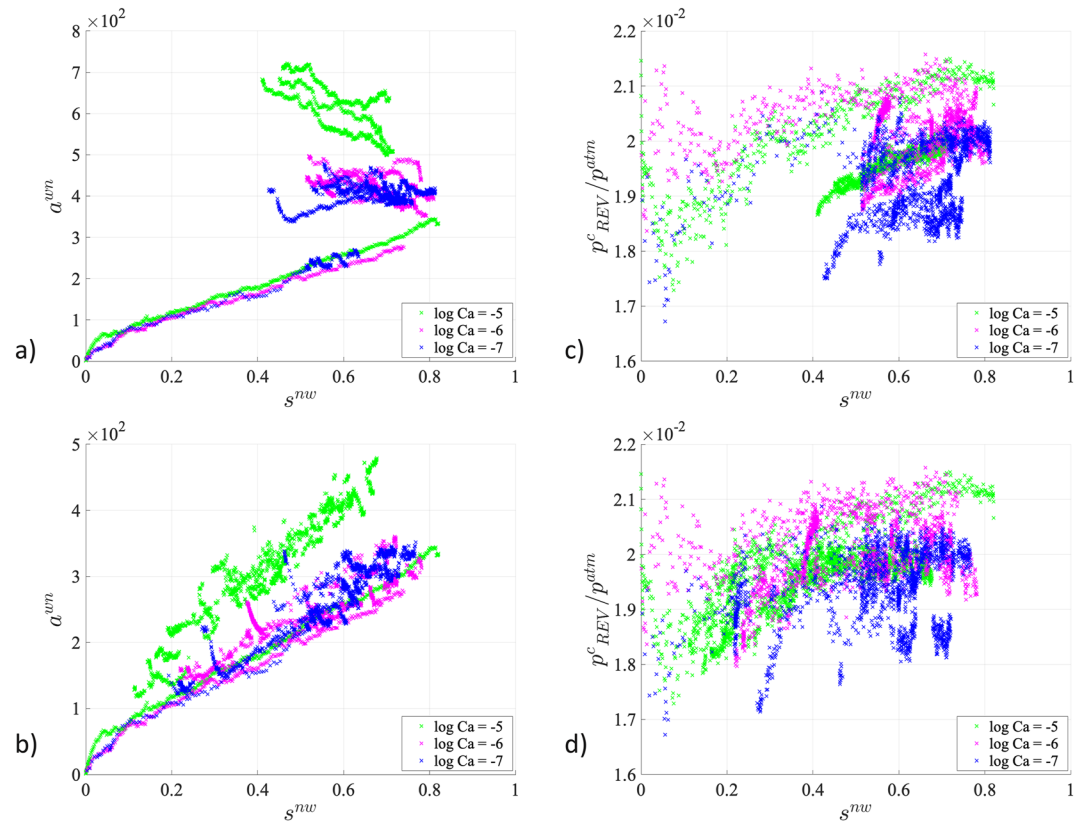


**Figure 5.** Data gathered from the images: Specific interfacial area vs. saturation for (a) all clusters, and (b) connected clusters, and capillary pressure vs. saturation for (c) all clusters, and (d) connected clusters.

that would be outside the scope of this work since this imaging approach for such flow experiments is not feasible in our facilities.

Given the limitations that we need to accommodate in our data processing, related to the nature of the porous medium itself, in Equation 7 the saturation of the invading fluid gets replaced by the saturation of the non-wetting phase, since drainage is the process of interest

$$a^{wn} = a(s^{nw})^b(1 - s^{nw})^c \left( \frac{P_{REV}^c}{p^{atm}} \right)^d \quad (7)$$

The fitting is done in four different ways: (a) for each drainage process (six processes for each Ca number), (b) all drainage data points with the same Ca number, (c) combinations of two sequential Ca numbers, and (d) for all three Ca numbers. Since every drainage process starts from the final stage of the imbibition before it, the history of the flow is implicitly included in the images. The number of images processed for each experiment is 1,738, 1,686, and 1,664 images for the Ca numbers  $10^{-5}$ ,  $10^{-6}$ , and  $10^{-7}$ , respectively.

The same fitting procedure is carried out on the data points collected from all clusters in the displacement process and then repeated for the data of the connected clusters only. The goodness of fit and the fit parameters resulting from both procedures are estimated and compared, as shown in the following section.

### 3. Results

In Figures 5a–5b, 5d, the main variables used in Equation 7 are plotted versus the saturation for all clusters and connected clusters. It can be observed in Figures 5a and 5b that the interfacial area produced is similar in the experiments with the Ca numbers  $10^{-7}$  and  $10^{-6}$  but bigger in the fastest experiment with  $Ca = 10^{-5}$ . That is expected since the increased boundary flux induces stronger viscous effects creating a different phase distribution

**Table 2**  
Goodness of Fit ( $R^2$ ) for Drainage Processes From the Experiment With  $Ca = 10^{-6}$

	All clusters	Connected clusters
Primary drainage	0.997	0.997
Scanning curve	0.64	0.95
Scanning curve	0.86	0.95
Scanning curve	0.68	0.92
Scanning curve	0.80	0.95
Scanning curve	0.85	0.97
All data points <sup>a</sup>	0.79	0.86

<sup>a</sup>Accumulated data points from all six displacement processes.

and more interfaces to absorb the energy. Moreover, the scanning curves for both interfacial area and capillary pressure are not so pronouncedly dispersed for the connected clusters during various cycles in contrast to the data from all clusters, illustrating the effects of considering connectivity in capturing hysteretic behavior of the displacement processes.

A comparison between the commonly used theories (Brooks & Corey, 1964; Van Genuchten, 1980) and the extended theory of two-phase flow in porous media (Hassanzadeh & Gray, 1990, 1993) shows that including the interfacial area in the closure equations has introduced a substantial improvement in capturing hysteresis, albeit depending on the boundary conditions. This study takes it a step further and shows that considering the connectivity of phases to their boundaries can expand the validity of this theory for a range of the  $Ca$  numbers and transient flow conditions.

As described in Section 2, a function (Equation 7) is fitted to two sets of data, one including the saturation, capillary pressure, and specific interfacial area of the whole non-wetting phase during a drainage displacement process and the other with the same variables but for the clusters of non-wetting phase connected to the boundary. Table 2 provides the  $R^2$  as a measure of goodness of fit for each displacement process belonging to the experiment with  $Ca$  number  $10^{-6}$  as an example. As one can see in every process, there is an improvement in the fitting when only the connected clusters are considered. Likewise, the fitting improves for cumulative data, including data points from the six drainage processes in one experiment with the same  $Ca$  number.

Moreover, in primary drainage, one can observe no improvement or, better to say, the inclusion of only the interfacial area for all clusters produces a very nice fit. This can mainly be attributed to the fact that it is not expected to have a significant occurrence of disconnections for the non-wetting phase during primary drainage.

As mentioned in Section 2.4, the same procedure is applied to the data from the three experiments, and fitting is improved when only the connected clusters are considered compared to the data for all clusters. Since we are interested in a function that can describe displacement processes, regardless of the  $Ca$  numbers, we will concentrate on all data points from each experiment (including six drainage processes). In Table 3, we list the  $R^2$  for the collective data of each  $Ca$  number, two consecutive  $Ca$  numbers combined, and all of the three experiments together. Although an improvement is observed in every case, in the combinations with the highest  $Ca$  number ( $Ca = 10^{-5}$ ), the fitting is not satisfactory.

By fitting Equation 7, we gather the parameters  $a$ ,  $b$ ,  $c$ , and  $d$ , which are presented in Table 4. By taking a closer look at the parameters, one can see that parameters  $b$ ,  $c$ , and  $d$  take values in a narrow range for both connected clusters and all clusters included. In an attempt to come up with a single function for all of the experimental data gathered in our experiments, with respect to the phase-connectivity concept, parameters  $b$ ,  $c$ , and  $d$  are fixed, and the goodness of fit is compared again to see how extensive fitting is affected by reducing the fitting parameters.

Moreover, the effect of fixing parameters  $b$ ,  $c$ , and  $d$  on the parameter  $a$  is studied. The values assigned to parameters  $b$ ,  $c$ , and  $d$  are the average of the values listed in Table 4, for all clusters and connected clusters separately. In other words, two functions as Equations 8 and 9 are fitted to the data for all clusters and the connected clusters respectively, and the fitting parameter  $a$ , as well as the goodness of the fit are recorded

$$a^{wn} = a(s^{nw})^{1.92}(1 - s^{nw})^{1.02} \left( \frac{p_{REV}^c}{p^{atm}} \right)^{-2.8}, \quad (8)$$

**Table 3**  
Goodness of Fit ( $R^2$ ) for Accumulative Data in Single Experiments and Their Combinations

Log (Ca)							
		-7	-6	-5	-7 and -6	-6 and -5	-7 and -6 and -5
$R^2$	All clusters	0.67	0.79	0.74	0.66	0.72	0.48
	Connected clusters	0.94	0.86	0.86	0.90	0.74	0.70

**Table 4**  
Function Parameters  $a, b, c, d$  Resulting in the Best Fit

Log (Ca)								
		-7	-6	-5	-7 and -6	-6 and -5	-7 and -6 and -5	Arithmetic mean
$a$	All clusters	0.24	0.05	0.06	26.54	4e-5	0.02	4.48
	Connected clusters	0.41	8.4	0.04	3.75	4e-4	0.05	2.1
$b$	All clusters	1.08	1.98	2.98	1.59	2.11	1.75	1.92
	Connected clusters	0.77	0.75	0.97	0.76	1.07	0.88	0.87
$c$	All clusters	0.16	0.93	2.09	0.61	1.29	1.03	1.02
	Connected clusters	-0.08	0.06	0.23	0.003	0.36	0.23	0.13
$d$	All clusters	-2.03	-2.81	-3.22	-1.03	-4.76	-3.06	-2.8
	Connected clusters	-1.73	-1	-2.5	-1.19	-3.71	-2.38	-2.1

$$a^{wn} = a(s^{nw})^{0.87} (1 - s^{nw})^{0.13} \left( \frac{p_{REV}^c}{p^{am}} \right)^{-2.1} \quad (9)$$

We observe that the goodness of fit changes only about 2% for connected clusters if we reduce the fitting parameters from four to one by assigning certain values to parameters  $b, c,$  and  $d$  ( $b = 0.87, c = 0.13,$  and  $d = -2.1$ ). Nevertheless, if we fix  $b = 1.92, c = 1.02,$  and  $d = -2.8$  for the experimental data, including all of the clusters, the goodness of fit would drop on average by 10%. See Table 5.

In Table 6, the values of parameter  $a,$  resulting from fitting a function with fixed  $b, c,$  and  $d$  are listed. The trend in the values of parameter  $a$  in the experiments shows its dependency on the Ca number, also interpretable as the transient effects in the displacement process.

#### 4. Discussion

In the literature, there is a plethora of experimental, numerical, and theoretical works revolving around the apparent hysteretic behavior of cyclic drainage and imbibition events. Two of the objectives have been the identification of underlying mechanisms and causes and to find an effective way of modeling hysteresis. Regarding the second objective, it is important for the approach to be practically applicable, and not only from a fundamental perspective. In this work we have focused our attention on the theories developed by Hassanizadeh and Gray (1990, 1993) and Hilfer (2006a, 2006b) are developed. In particular, we attempt to merge these two modeling approaches. One theory (Hassanizadeh & Gray, 1990, 1993) considers the interfacial area to be a new state variable in two-phase flow (in addition to saturation and capillary pressure), and the other (Hilfer, 2006a, 2006b) discriminates between connected and disconnected (or percolating and non-percolating) parts of a phase and introduce corresponding saturations for each phase as state variables. We perform sequential displacement experiments to test the possibility of combining the two modeling approaches into one. We then evaluate the role of the connected phase saturation on the production of three-dimensional surfaces between saturation, capillary pressure, and interfacial area as state variables. Our quantitative results clearly show that taking only the connected saturation into account allows us to capture hysteresis more effectively than considering the total saturation without any distinction for its connectivity. To that end, we use a physically consistent fitting function, as shown in Equation 6. Our results show that the synthesis of the theories proposed by Hassanizadeh and Gray (1990, 1993) and Hilfer (2006a, 2006b)

**Table 5**  
Goodness of Fit ( $R^2$ ) for All Data in Single Experiments and Their Combinations for Equations 8 and 9

Log (Ca)							
		-7	-6	-5	-7 and -6	-6 and -5	-7 and -6 and -5
$R^2$	All clusters	0.38	0.78	0.68	0.5	0.65	0.47
	Connected clusters	0.91	0.82	0.86	0.88	0.70	0.68

**Table 6**  
Values of Parameter  $a$  in Equations 8 and 9 Resulting in the Best Fit for Various  $Ca$  Numbers and Their Combinations

Log (Ca)							
		-7	-6	-5	-7 and -6	-6 and -5	-7 and -6 and -5
a	All clusters	0.042	0.050	0.065	0.045	0.059	0.053
	Connected clusters	0.13	0.13	0.17	0.13	0.15	0.14

provides a more efficient description of the evolution of two-phase flow under any boundary conditions. In other words, an extended continuum-based model that takes the interfacial area as a state variable into account includes the hysteresis more expeditiously if the connectivity of the phase is also considered.

The inherent advantage of microfluidics, that is, the real-time visualization of two-phase flow processes, enables us to differentiate in a robust way between connected to the boundary phases, or not, and quantify their contribution to the constitutive surface of saturation, capillary pressure, and specific interfacial area. Under conditions where there is no remobilization of the disconnected phases, for each displacement event the porous medium is effectively different. This justifies the need to quantify phase connectivity explicitly, knowing that after a number of cycles, the configuration of the phases eventually reaches a steady state. This has enhanced our understanding of the physical effects involved, and also made evident the correlation between the boundary conditions and the relative importance of the pore geometry. In this way we are able to highlight the importance of accounting, at the macroscale level, for the variations in pore-scale distribution of phases under different transient conditions varying from capillary-dominated to viscous-dominated flow regimes. It is also important to investigate the potential of Euler characteristic number and its evolution modeling hysteresis using our extensive pore-scale data set. To pursue this investigation, 2D formulation of the Euler characteristic number should be adjusted and connectivity of the wetting phase should be carefully characterized.

There several issues and challenges regarding interpreting the presented results. One of the challenges is the cross-section of the pores and its effect on the behavior of the fluids. Due to the chemical etching method of manufacturing of the microfluidic cell, there is a sharp corner at the top of the channels while a curved corner at the bottom exists. This feature of the channels strongly affects the interpretation of results, as mentioned in Section 2.4. The flow channel shape, along with the wetting properties of the material, creates significant corner/film flow of the wetting phase while preventing it from being captured in the images through the shadow it causes. The wetting phase seems to be connected via paths of variable connectivity (reflected in the response times), while the extents of the connection remain unknown. Given this and the consequences of a doubtful consideration regarding the connectivity of wetting phase, we have decided to exclude imbibition data from our analysis.

The curvature on the walls of the flow network introduces another issue related to the degree of freedom in consideration of a contact angle in the  $z$ -direction. We believe that the approach of adopting the mean planar contact angle as the one for the  $z$ -direction does not deviate significantly from the actual case. Nevertheless, 3D imaging would be highly beneficial and is one of the things we anticipate doing in the near future. To address these issues, we plan to perform similar experiments in microfluidic cells made of Poly-Di-Methyl-Siloxane with simpler in-depth geometry and better-defined wetting phase connectivity.

In this work, we show that considering only the connected phase and the corresponding interfacial area significantly improves the potential of modeling hysteresis. However, the fact that the efficiency of this approach gets reduced by combining higher volumetric fluxes in the datasets, which result in dynamic conditions as also shown in Karadimitriou et al. (2014), implies that other factors need to be considered. Given the increasing competition between capillary and viscous effects for increasing  $Ca$  numbers or boundary fluxes, we speculate that the geometrical features of the porous structure itself become gradually important. The tortuosity of the porous structure and some local characteristics on the pore scale, like confinements or constrains in the pore space, which drastically influence the pore-scale  $Ca$  number, need to be addressed in detail under highly dynamic conditions so as for their effect to be evaluated. We anticipate that in our future work, these issues will be addressed.

## Data Availability Statement

The datasets are available in the Data Repository of the University of Stuttgart. In the data set, Vahid Dastjerdi et al. (2022) provide images of optical microscopy (\*.tif) together with the pressure data (\*.csv). Moreover, the CAD design of the microfluidic cell is available.

## Acknowledgments

This work is funded by Deutsche Forschungsgemeinschaft (DFG, German Research Foundation) under Germany's Excellence Strategy—EXC 2075–390740016. We acknowledge the support by the Stuttgart Center for Simulation Science (SimTech). Open Access funding enabled and organized by Projekt DEAL.

## References

- Alvarado, V., & Manrique, E. (2010). *Enhanced oil recovery concepts*. Gulf Professional Publishing.
- Armstrong, R. T., McClure, J. E., Berrill, M. A., Rücker, M., Schlüter, S., & Berg, S. (2016). Beyond Darcy's law: The role of phase topology and ganglion dynamics for two-fluid flow. *Physical Review E - Statistical Physics, Plasmas, Fluids, and Related Interdisciplinary Topics*, *94*(4), 043113. <https://doi.org/10.1103/physreve.94.043113>
- Armstrong, R. T., McClure, J. E., Robins, V., Liu, Z., Arns, C. H., Schlüter, S., & Berg, S. (2019). Porous media characterization using minkowski functionals: Theories, applications and future directions. *Transport in Porous Media*, *130*(1), 305–335. <https://doi.org/10.1007/s11242-018-1201-4>
- Armstrong, R. T., Porter, M. L., & Wildenschild, D. (2012). Linking pore-scale interfacial curvature to column-scale capillary pressure. *Advances in Water Resources*, *46*, 55–62. <https://doi.org/10.1016/j.advwatres.2012.05.009>
- Bachu, S. (2000). Sequestration of CO<sub>2</sub> in geological media: Criteria and approach for site selection in response to climate change. *Energy Conversion and Management*, *41*(9), 953–970. [https://doi.org/10.1016/s0196-8904\(99\)00149-1](https://doi.org/10.1016/s0196-8904(99)00149-1)
- Bartels, W. B., Rücker, M., Boone, M., Bultreys, T., Mahani, H., Berg, S., et al. (2019). Imaging spontaneous imbibition in full Darcy-scale samples at pore-scale resolution by fast X-ray tomography. *Water Resources Research*, *55*(8), 7072–7085. <https://doi.org/10.1029/2018wr024541>
- Bear, J. (1972). *Dynamics of fluids in porous media*. American Elsevier Publishing Company.
- Benson, S. M., & Cole, D. R. (2008). CO<sub>2</sub> sequestration in deep sedimentary formations. *Elements*, *4*(5), 325–331. <https://doi.org/10.2113/gselements.4.5.325>
- Brooks, R. H., & Corey, A. T. (1964). Hydraulic properties of porous media.
- Chen, D., Pyrak-Nolte, L. J., Griffin, J., & Giordano, N. J. (2007). Measurement of interfacial area per volume for drainage and imbibition. *Water Resources Research*, *43*(12), W12504. <https://doi.org/10.1029/2007wr006021>
- Cheng, J. T., Pyrak-Nolte, L. J., Nolte, D. D., & Giordano, N. J. (2004). Linking pressure and saturation through interfacial areas in porous media. *Geophysical Research Letters*, *31*(8), L08502. <https://doi.org/10.1029/2003gl019282>
- Chernov, N. (2021). *Circle fit (Pratt method)*. MATLAB Central File Exchange.
- Culligan, K. A., Wildenschild, D., Christensen, B. S. B., Gray, W. G., Rivers, M. L., & Tompson, A. F. B. (2004). Interfacial area measurements for unsaturated flow through a porous medium. *Water Resources Research*, *40*(12), W12413. <https://doi.org/10.1029/2004wr003278>
- Damodara, S., Shahriari, S., Wu, W.-I., Rezai, P., Hsu, H.-H., & Selvaganapathy, R. (2021). 1 - Materials and methods for microfabrication of microfluidic devices. In X. Li, & Y. Zhou (Eds.), *Microfluidic devices for biomedical applications* (2nd ed., pp. 1–78). Woodhead Publishing.
- Doster, F., & Hilfer, R. (2014). A comparison between simulation and experiment for hysteretic phenomena during two-phase immiscible displacement. *Water Resources Research*, *50*(1), 681–686. <https://doi.org/10.1002/2013wr014619>
- Gao, H., Tatomir, A. B., Karadimitriou, N. K., Steeb, H., & Sauter, M. (2021). A two-phase, pore-scale reactive transport model for the kinetic interface-sensitive tracer. *Water Resources Research*, *57*(6), e2020WR028572. <https://doi.org/10.1029/2020wr028572>
- Gray, W. G., & Hassanizadeh, S. M. (1989). Averaging theorems and averaged equations for transport of interface properties in multiphase systems. *International Journal of Multiphase Flow*, *15*(1), 81–95. [https://doi.org/10.1016/0301-9322\(89\)90087-6](https://doi.org/10.1016/0301-9322(89)90087-6)
- Hassanizadeh, M., & Gray, W. G. (1979). General conservation equations for multi-phase systems: 1. Averaging procedure. *Advances in Water Resources*, *2*, 131–144. [https://doi.org/10.1016/0309-1708\(79\)90025-3](https://doi.org/10.1016/0309-1708(79)90025-3)
- Hassanizadeh, S. M. (2015). Advanced theories of two-phase flow in porous media. In (p. 47–62).
- Hassanizadeh, S. M., & Gray, W. G. (1990). Mechanics and thermodynamics of multiphase flow in porous media including interphase boundaries. *Advances in Water Resources*, *13*(4), 169–186. [https://doi.org/10.1016/0309-1708\(90\)90040-b](https://doi.org/10.1016/0309-1708(90)90040-b)
- Hassanizadeh, S. M., & Gray, W. G. (1993). Thermodynamic basis of capillary pressure in porous media. *Water Resources Research*, *29*(10), 3389–3405. <https://doi.org/10.1029/93wr01495>
- Held, R. J., & Celia, M. A. (2001). Modeling support of functional relationships between capillary pressure, saturation, interfacial area and common lines. *Advances in Water Resources*, *24*(3–4), 325–343. [https://doi.org/10.1016/s0309-1708\(00\)0060-9](https://doi.org/10.1016/s0309-1708(00)0060-9)
- Herring, A. L., Harper, E. J., Andersson, L., Sheppard, A., Bay, B. K., & Wildenschild, D. (2013). Effect of fluid topology on residual nonwetting phase trapping: Implications for geologic CO<sub>2</sub> sequestration. *Advances in Water Resources*, *62*, 47–58. <https://doi.org/10.1016/j.advwatres.2013.09.015>
- Herring, A. L., Middleton, J., Walsh, R., Kingston, A., & Sheppard, A. (2017). Flow rate impacts on capillary pressure and interface curvature of connected and disconnected fluid phases during multiphase flow in sandstone. *Advances in Water Resources*, *107*, 460–469. <https://doi.org/10.1016/j.advwatres.2017.05.011>
- Herring, A. L., Robins, V., & Sheppard, A. P. (2019). Topological persistence for relating microstructure and capillary fluid trapping in sandstones. *Water Resources Research*, *55*(1), 555–573. <https://doi.org/10.1029/2018wr022780>
- Hilfer, R. (2006a). Capillary pressure, hysteresis and residual saturation in porous media. *Physica A: Statistical Mechanics and its Applications*, *359*, 119–128. <https://doi.org/10.1016/j.physa.2005.05.086>
- Hilfer, R. (2006b). Macroscopic capillarity and hysteresis for flow in porous media. *Physical Review E*, *73*(1), 016307. <https://doi.org/10.1103/physreve.73.016307>
- Hilfer, R., Armstrong, R. T., Berg, S., Georgiadis, A., & Ott, H. (2015). Capillary saturation and desaturation. *Physical Review E*, *92*(6), 063023. <https://doi.org/10.1103/physreve.92.063023>
- Hilfer, R., & Doster, F. (2010). Percolation as a basic concept for macroscopic capillarity. *Transport in Porous Media*, *82*(3), 507–519. <https://doi.org/10.1007/s11242-009-9395-0>
- Joekar-Niasar, V., Doster, F., Armstrong, R. T., Wildenschild, D., & Celia, M. A. (2013). Trapping and hysteresis in two-phase flow in porous media: A pore-network study. *Water Resources Research*, *49*(7), 4244–4256. <https://doi.org/10.1002/wrcr.20313>
- Joekar-Niasar, V., & Hassanizadeh, S. M. (2011). Specific interfacial area: The missing state variable in two-phase flow equations? *Water Resources Research*, *47*(5), W05513. <https://doi.org/10.1029/2010wr009291>

- Joekar-Niasar, V., & Hassanizadeh, S. M. (2012). Uniqueness of specific interfacial area–capillary pressure–saturation relationship under non-equilibrium conditions in two-phase porous media flow. *Transport in Porous Media*, 94(2), 465–486. <https://doi.org/10.1007/s11242-012-9958-3>
- Joekar-Niasar, V., Hassanizadeh, S. M., & Leijnse, A. (2008). Insights into the relationships among capillary pressure, saturation, interfacial area and relative permeability using pore-network modeling. *Transport in Porous Media*, 74(2), 201–219. <https://doi.org/10.1007/s11242-007-9191-7>
- Karadimitriou, N. K., Hassanizadeh, S. M., Joekar-Niasar, V., & Kleingeld, P. (2014). Micromodel study of two-phase flow under transient conditions: Quantifying effects of specific interfacial area. *Water Resources Research*, 50(10), 8125–8140. <https://doi.org/10.1002/2014wr015388>
- Karadimitriou, N. K., Joekar-Niasar, V., Hassanizadeh, S. M., Kleingeld, P. J., & Pyrak-Nolte, L. J. (2012). A novel deep reactive ion etched (DRIE) glass micro-model for two-phase flow experiments. *Lab on a Chip*, 12(18), 3413–3418. <https://doi.org/10.1039/c2lc40530j>
- Karadimitriou, N. K., Musterd, M., Kleingeld, P. J., Kreutzer, M. T., Hassanizadeh, S. M., & Joekar-Niasar, V. (2013). On the fabrication of PDMS micromodels by rapid prototyping, and their use in two-phase flow studies. *Water Resources Research*, 49(4), 2056–2067. <https://doi.org/10.1002/wrcr.20196>
- Marle, C.-M. (1982). On macroscopic equations governing multiphase flow with diffusion and chemical reactions in porous media. *International Journal of Engineering Science*, 20(5), 643–662. [https://doi.org/10.1016/0020-7225\(82\)90118-5](https://doi.org/10.1016/0020-7225(82)90118-5)
- MATLAB® (2019). MATLAB version 9.6.0.1214997 (R2019b)[Computer Software manual]. *The MathWorks Inc.*
- McClure, J. E., Armstrong, R. T., Berrill, M. A., Schlüter, S., Berg, S., Gray, W. G., & Miller, C. T. (2018). Geometric state function for two-fluid flow in porous media. *Physical Review Fluids*, 3(8), 084306. <https://doi.org/10.1103/physrevfluids.3.084306>
- McClure, J. E., Berrill, M. A., Gray, W. G., & Miller, C. T. (2016). Influence of phase connectivity on the relationship among capillary pressure, fluid saturation, and interfacial area in two-fluid-phase porous medium systems. *Physical Review E - Statistical Physics, Plasmas, Fluids, and Related Interdisciplinary Topics*, 94(3), 033102. <https://doi.org/10.1103/physreve.94.033102>
- McClure, J. E., Ramstad, T., Li, Z., Armstrong, R. T., & Berg, S. (2020). Modeling geometric state for fluids in porous media: Evolution of the Euler characteristic. *Transport in Porous Media*, 133(2), 229–250. <https://doi.org/10.1007/s11242-020-01420-1>
- Mecke, K., & Arns, C. H. (2005). Fluids in porous media: A morphometric approach. *Journal of Physics: Condensed Matter*, 17(9), S503–S534. <https://doi.org/10.1088/0953-8984/17/9/014>
- Miller, C. T., Bruning, K., Talbot, C. L., McClure, J. E., & Gray, W. G. (2019). Nonhysteretic capillary pressure in two-fluid porous medium systems: Definition, evaluation, validation, and dynamics. *Water Resources Research*, 55(8), 6825–6849. <https://doi.org/10.1029/2018wr024586>
- Muggeridge, A., Cockin, A., Webb, K., Frampton, H., Collins, I., Moulds, T., & Salino, P. (2014). Recovery rates, enhanced oil recovery and technological limits. *Philosophical transactions. Series A, Mathematical, Physical, and Engineering Sciences*, 372(2006), 20120320. <https://doi.org/10.1098/rsta.2012.0320>
- Niessner, J., & Hassanizadeh, S. M. (2008). A model for two-phase flow in porous media including fluid-fluid interfacial area. *Water Resources Research*, 44(8), 006721. <https://doi.org/10.1029/2007wr006721>
- Niessner, J., & Hassanizadeh, S. M. (2009). Non-equilibrium interphase heat and mass transfer during two-phase flow in porous media—Theoretical considerations and modeling. *Advances in Water Resources*, 32(12), 1756–1766. <https://doi.org/10.1016/j.advwatres.2009.09.007>
- Ott, H., Kharrat, A., Borji, M., & Arnold, P. (2020). Fluid-phase topology of complex displacements in porous media. *Physical Review Research*, 2, 023240. <https://doi.org/10.1103/physrevresearch.2.023240>
- Powers, S. E., Abriola, L. M., & Weber, W. J. (1992). An experimental investigation of nonaqueous phase liquid dissolution in saturated subsurface systems: Steady state mass transfer rates. *Water Resources Research*, 28(10), 2691–2705. <https://doi.org/10.1029/92wr00984>
- Pratt, V. (1987). Direct least-squares fitting of algebraic surfaces. *Computer Graphics*, 21(4), 145–152. <https://doi.org/10.1145/37402.37420>
- Pyrak-Nolte, L. J., Nolte, D. D., Chen, D., & Giordano, N. J. (2008). Relating capillary pressure to interfacial areas. *Water Resources Research*, 44(6), W06408. <https://doi.org/10.1029/2007wr006434>
- Quintard, M., & Whitaker, S. (1994). Convection, dispersion, and interfacial transport of contaminants: Homogeneous porous media. *Advances in Water Resources*, 17(4), 221–239. [https://doi.org/10.1016/0309-1708\(94\)90002-7](https://doi.org/10.1016/0309-1708(94)90002-7)
- Schlüter, S., Berg, S., Rücker, M., Armstrong, R. T., Vogel, H.-J., Hilfer, R., & Wildenschild, D. (2016). Pore-scale displacement mechanisms as a source of hysteresis for two-phase flow in porous media. *Water Resources Research*, 52(3), 2194–2205. <https://doi.org/10.1002/2015wr018254>
- Spiteri, E. J., Juanes, R., Blunt, M. J., & Orr, F. M. (2008). A new model of trapping and relative permeability hysteresis for all wettability characteristics. *SPE Journal*, 13(03), 277–288. <https://doi.org/10.2118/96448-pa>
- Tsakiroglou, C. D., Theodoropoulou, M. A., & Karoutsos, V. (2003). Nonequilibrium capillary pressure and relative permeability curves of porous media. *AIChE Journal*, 49(10), 2472–2486. <https://doi.org/10.1002/aic.690491004>
- Vahid Dastjerdi, S., Karadimitriou, N. K., & Steeb, H. (2022). Data for: Experimental evaluation of connectivity in two-phase flow in porous media during drainage [Dataset]. DaRUS. Retrieved from: <https://doi.org/10.18419/darus-2250>
- Van Genuchten, M. (1980). A closed-form equation for predicting the hydraulic conductivity of unsaturated soils. *Soil Science Society of America Journal*, 44(5), 892–898. <https://doi.org/10.2136/sssaj1980.03615995004400050002x>
- Weinhardt, F., Class, H., Vahid Dastjerdi, S., Karadimitriou, N. K., Lee, D., & Steeb, H. (2021). Experimental methods and imaging for enzymatically induced calcite precipitation in a microfluidic cell. *Water Resources Research*, 57(3), e2020WR029361. <https://doi.org/10.1029/2020wr029361>
- Whitaker, S. (2013). *The method of volume averaging* (Vol. 13). Springer Science & Business Media.
- White, C. M., Strazisar, B. R., Granite, E. J., Hoffman, J. S., & Pennline, H. W. (2003). Separation and capture of CO<sub>2</sub> from large stationary sources and sequestration in geological formations, coalbeds and deep saline aquifers. *Journal of the Air & Waste Management Association*, 53(6), 645–715. <https://doi.org/10.1080/10473289.2003.10466206>
- Yiotis, A., Karadimitriou, N. K., Zarihos, I., & Steeb, H. (2021). Pore-scale effects during the transition from capillary-to viscosity-dominated flow dynamics within microfluidic porous-like domains. *Scientific Reports*, 11(1), 3891. <https://doi.org/10.1038/s41598-021-83065-8>
- Zhuang, L., Bezerra Coelho, C., Hassanizadeh, S., & van Genuchten, M. (2017). Analysis of the hysteretic hydraulic properties of unsaturated soil. *Vadose Zone Journal*, 16(5), vj2016.11.0115. <https://doi.org/10.2136/vzj2016.11.0115>
- Zhuang, L., Hassanizadeh, S. M., Qin, C.-Z., & de Waal, A. (2017). Experimental investigation of hysteretic dynamic capillarity effect in unsaturated flow. *Water Resources Research*, 53(11), 9078–9088. <https://doi.org/10.1002/2017wr020895>